THE ASTRONOMICAL JOURNAL, 125:2411–2426, 2003 May
© 2003. The American Astronomical Society. All rights reserved. Printed in U.S.A.

THE *SIRTF* FIRST-LOOK SURVEY. I. VLA IMAGE AND SOURCE CATALOG

J. J. CONDON, W. D. COTTON, AND Q. F. YIN
National Radio Astronomy Observatory,[1] 520 Edgemont Road, Charlottesville, VA 22903;
jcondon@nrao.edu, bcotton@nrao.edu, qyin@nrao.edu

D. L. SHUPE, L. J. STORRIE-LOMBARDI, G. HELOU, AND B. T. SOIFER
SIRTF Science Center, 314-6, California Institute of Technology, 1200 East California Boulevard, Pasadena, CA 91125;
shupe@ipac.caltech.edu, lisa@ipac.caltech.edu, gxh@ipac.caltech.edu, bts@mop.caltech.edu

AND

M. W. WERNER
Jet Propulsion Laboratory, California Institute of Technology, 4800 Oak Grove Drive, Pasadena, CA 91109;
mww@ipac.caltech.edu
Received 2003 January 27; accepted 2003 February 5

ABSTRACT

The First-Look Survey (FLS) of the *Space Infrared Telescope Facility* (*SIRTF*) will cover about 5 deg^2 centered on J2000.0 $\alpha = 17^h18^m$, $\delta = +59°30'$ in order to characterize the extragalactic infrared sky 2 orders of magnitude deeper than the *IRAS* survey. We expect that most of the FLS far-infrared ($\lambda = 160$, 70, and 24 μm) sources will be star-forming galaxies obeying the very tight far-infrared/radio correlation and will be continuum radio sources with flux densities $S \gtrsim 100$ μJy at $\nu = 1.4$ GHz. Conversely, radio sources stronger than 100 μJy are usually powered by star-forming galaxies, plus some active galactic nuclei, and most should be detectable by the *SIRTF* FLS. Thus, a sensitive radio survey can be used to select and identify most of the *SIRTF* FLS source population before launch. We used the B configuration of the VLA to make an image of the FLS area at $\nu = 1.4$ GHz with $\sigma \approx 23$ μJy beam^{-1} rms fluctuations, $\theta = 5''.0$ resolution, and $\sigma_\alpha \approx \sigma_\delta \lesssim 0''.5$ rms uncertainties in right ascension and declination. The resulting radio image and catalog of 3565 radio components with peak flux densities $S_p \geq 5\,\sigma = 115$ μJy beam^{-1} have been released via the Web to expedite follow-up optical identification and spectroscopy.

Key words: catalogs — galaxies: active — galaxies: starburst — infrared radiation — radio continuum — surveys

On-line material: machine-readable table

1. INTRODUCTION

The *Space Infrared Telescope Facility* (*SIRTF*) is the fourth and final element in NASA's family of "Great Observatories." Its 0.85 m telescope and three cryogenically cooled science instruments are capable of performing imaging and spectroscopy in the 3–180 μm wavelength range. Incorporating the latest in large-format infrared detector arrays, *SIRTF* offers orders-of-magnitude improvements in sensitivity and area coverage over earlier programs. While *SIRTF*'s mission lifetime requirement remains 2.5 yr, recent programmatic and engineering developments have brought a 5 yr cryogenic mission within reach. It is currently scheduled for launch into solar orbit in 2003 April.

Following the loss of the *Wide-Field Infrared Explorer* mission, a special advisory committee chaired by R. Williams recommended that *SIRTF* conduct a First-Look Survey (FLS) using about 100 hr of telescope time to characterize the infrared sky 2 orders of magnitude deeper than *IRAS* reached. The FLS[2] is essential for effective use of *SIRTF* mission time because so little is known about faint infrared sources and the cirrus foreground at these levels. A community workshop was convened by B. T. S., at the *SIRTF* Science Center, at Caltech on 1999 September 15 and 16 to define the FLS. The resulting extragalactic FLS should

1. Detect enough extragalactic sources at unexplored sensitivity levels to generate a representative sample and reduce the uncertainties in the source counts;
2. Characterize the dominant source populations with both the MIPS ($\lambda = 160$, 70, and 24 μm) and IRAC ($\lambda = 8.0$, 5.8, 4.5, and 3.6 μm) detectors from *SIRTF* plus ancillary optical, near-infrared, and radio surveys; and
3. Explore the moderately high-$|b|$ cirrus foreground and its effect on point-source detectability.

All of this done in time to support the first *SIRTF* science proposals. The planned FLS consists of a "shallow" survey covering 5 deg^2 and a 2–3 times deeper "verification" survey of 0.25 deg^2 inside the shallow survey area. The shallow survey is expected to have 5 σ detection limits of 25, 3.0, and 0.5 mJy and detect about 400, 1500, and 2500 sources at $\lambda = 160$, 70, and 24 μm, respectively. Source confusion is likely to limit the sensitivity at $\lambda = 160$ and 70 μm, so the detection limits at these wavelengths are uncertain and model dependent. The IRAC sensitivity limits will be 49, 43, 15, and 12 μJy at 8.0, 5.8, 4.5, and 3.6 μm, respectively. The *Infrared Space Observatory* FIRBACK survey (Puget et al. 1999) at $\lambda = 175$ μm suggests that the FLS will be dominated by a large and strongly evolving population of starburst galaxies at cosmological redshifts, supplemented by a smaller but still significant number of active galactic nuclei (AGNs).

[1] The National Radio Astronomy Observatory is a facility of the National Science Foundation operated under cooperative agreement by Associated Universities, Inc.

[2] See http://sirtf.caltech.edu/SSC/fls/.

Optical and radio surveys are an essential part of the FLS. Optical identifications are the first step toward understanding FLS sources. If local *IRAS* sources with the highest far-infrared/optical flux ratios (Arp 220, for example) were moved to cosmological distances where they would be just above the FLS sensitivity detection limit, they would still be brighter than $R \approx 25.5$ mag. Optical images of this depth were obtained with the CCD Mosaic camera on the NOAO 4 m telescope in 2000 May. Accurate (rms errors $\sigma_\alpha \approx \sigma_\delta < 1''$ in right ascension and declination) positions are needed to make complete and reliable associations of infrared or radio sources with such faint galaxies. However, most of the detected MIPS sources will have flux densities near the 5 σ detection limit, so their rms positional uncertainties in each coordinate will be about 10% of the half-intensity beamwidths (Condon 1997): $\sigma_\alpha \approx \sigma_\delta \approx 2''$ at $\lambda = 70\ \mu$m, and $\sigma_\alpha \approx \sigma_\delta \approx 5''$ at $\lambda = 160\ \mu$m.

A deep radio image covering the FLS area is needed for two reasons: (1) Nearly all far-infrared (FIR) sources obey the tight FIR/radio flux correlation (Condon, Anderson, & Helou 1991), and most radio sources fainter than 1 mJy at 1.4 GHz also appear to be starburst galaxies obeying the FIR/radio correlation (Condon 1989). Thus, we expect that the deep FIR and radio source populations are nearly identical. Only radio observations can provide prelaunch images and catalogs that both select most of the several thousand galaxies that will appear in the FIR images and reject the millions of galaxies brighter than $R \approx 25.5$ that will not. (2) The radio image can have the higher resolution and positional accuracy required for making reliable optical identifications on the basis of position coincidence alone. The radio data can be used to select and identify those optical galaxies most likely to be FLS sources for further study before launch. Later, the FIR/radio flux ratios can also be used to distinguish dust-shrouded, radio-loud AGN from dusty starburst galaxies.

Only the VLA B configuration operating at $\nu \approx 1.4$ GHz can efficiently produce radio images with the required sky coverage, sensitivity, and resolution. If the primary beam is a circular Gaussian with FWHM ϕ, the effective field of view $\Omega_e \approx \pi\phi^2/(8 \ln 2)$ for surveys is only half the primary-beam solid angle (Condon et al. 1998). Thus, $\Omega_e \approx \frac{1}{7}$ deg^2 for the $\phi \approx 31'$ primary beamwidth of the VLA at 1.4 GHz, and 35 partially overlapping fields are required to make a mosaic image covering the 5 deg^2 FLS area with nearly uniform sensitivity. The 1.4 GHz detection limits needed to match the MIPS shallow survey are 5 $\sigma \lesssim 100\ \mu$Jy. This estimate is based on the following assumptions: (1) $\langle S(60\ \mu\text{m})/S(1.4\ \text{GHz})\rangle \approx 140$ in the source frame, (2) most radio sources have spectral indexes $\alpha \approx 0.7$, (3) most FIR sources have the average spectra of sources in the *IRAS* bright galaxy sample (Soifer et al. 1989), and (4) the median redshift of the fainter FLS sources is $\langle z\rangle \lesssim 1$. The VLA can approach this sensitivity after about 7 hr of integration per field. The B configuration resolution is $5''$ FWHM (full width between half-maximum points), so the rms confusion $\sigma_c \approx 1\ \mu$Jy beam^{-1} is negligible, and even the faintest detectable (5 σ) sources will have $\sigma_\alpha \approx \sigma_\delta \approx 0\farcs5$ uncertainties in right ascension and declination.

The scientific value of the optical and radio surveys is greatest if they can be completed before launch. To ensure that the FLS area will be visible to *SIRTF* immediately after the in-orbit checkout, the FLS must be located inside the constant viewing zone (CVZ) within 10° of an ecliptic pole. In the northern CVZ, the region having the lowest cirrus brightness (1–2 MJy sr^{-1} at $\lambda = 100\ \mu$m) lies near J2000.0 $\alpha = 17^{\rm h}00^{\rm m}$, $\delta = +61°$ (Schlegel, Finkbeiner, & Davis 1998). The FLS center position $\alpha = 17^{\rm h}18^{\rm m}$, $\delta = +59°30'$ is offset slightly to avoid relatively strong ($S > 300$ mJy) radio sources whose sidelobes can degrade VLA images. Like the NRAO VLA Sky Survey (NVSS; Condon et al. 1998), the VLA portion of the FLS was made as a service to the astronomical community.[3]

2. VLA OBSERVATIONS AND DATA ANALYSIS

The area covered by the FLS is much larger than the VLA primary beam at $\nu = 1.4$ GHz, a Bessel function $\phi = 30\farcm83$ between half-power points, so we covered it by pointing at 35 positions selected from the NVSS pointing grid. The pointing centers and the boundary of the region covered by the final VLA image are shown in Figure 1.

The observations were made during two successive B configuration sessions of the VLA, 2001 February through May and 2002 June through August. We used the 4-IF mode, which provides right and left circular polarizations at both 1.365 GHz and 1.435 GHz. To minimize bandwidth smearing, each IF was divided into seven spectral channels of bandwidth 3.125 MHz. The nearby phase calibrator 1634+627 was observed about four times per hour to track atmospheric phase fluctuations closely, and the intensity calibrator 3C 286 was observed at the beginning of each observing run. The assumed flux densities of 3C 286 were $S(1.365\ \text{GHz}) = 15.01$ Jy and $S(1.435\ \text{GHz}) = 14.65$ Jy.

[3] The principal data products are available at the NRAO Web site http://www.cv.nrao.edu/sirtf_fls/ and at also at the *SIRTF* web site http://sirtf.caltech.edu/SSC/fls. They include FITS-format images, source catalogs, and user software for browsing the catalog and extracting postage-stamp subimages.

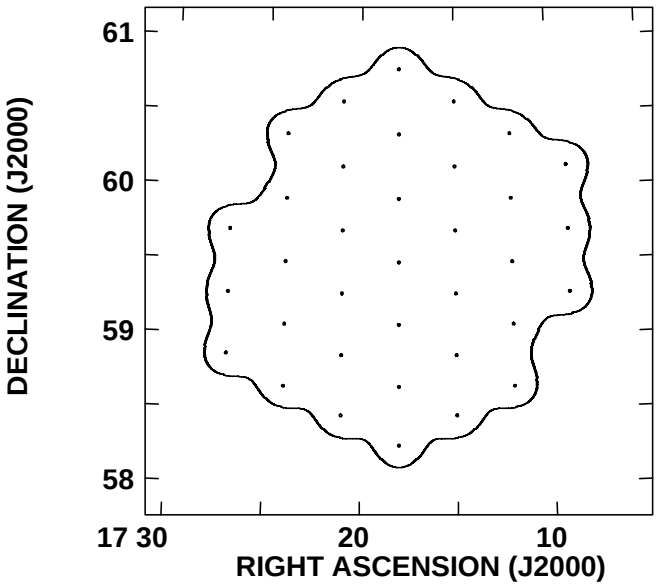

FIG. 1.—VLA covered the FLS area with a grid of 35 pointings (*points*). The individual images were mosaicked and the final image was blanked wherever its statistical weight fell below $W = 0.64$ (*curved boundary*). *Abscissa*: Right ascension (hours and minutes). *Ordinate*: Declination (degrees).

The calibrated and edited (u, v) data from each pointing were imaged separately with the special AIPS task VLALB. It incorporates many of the automatic imaging features from the NVSS imaging task VLAD (Condon et al. 1998). In addition, it accurately images the curved sky by breaking the main field of view, a spherical cap with radius 45′, into a fly's eye of $\sim 10^2$ smaller fields, each of which is a plane whose center is tangent to the spherical sky. After cleaning and restoration with a 5.″0 FWHM circular Gaussian beam, the small fields were flattened onto the final image plane. All but two of the 35 fields were imaged with ROBUST = 0.7 weighting, a compromise (u, v)-plane taper that reduces the sidelobes and increases the resolution of the natural dirty beam but multiplies the image noise by about 1.07. The two fields containing the brightest point sources were imaged with ROBUST = 0.5 for higher dynamic range.

The average integration time on one pointing position was about 5 hr. The theoretical rms fluctuation in a noise-limited naturally weighted image at each pointing center is about

$$\sigma = \frac{\sqrt{2} k_{\rm B} T_{\rm s}}{\eta_{\rm a} \eta_{\rm c} A \sqrt{N_b N_{\rm IF} \tau \Delta\nu}}$$

(Crane & Napier 1989), where $k_{\rm B} \approx 1.38 \times 10^{-23}$ J K^{-1} is the Boltzmann constant, $T_s \approx 40$ K is the system temperature at the typical zenith angle of our observations, $\langle z \rangle \approx 40^\circ$, $\eta_a = 0.51$ is the aperture efficiency, $\eta_c \approx 0.77$ is the correlator efficiency, A is the geometric area of one 25 m telescope, $N_b = 351$ is the number of baselines when all 27 telescopes are in the array, $N_{\rm IF} = 4$, $\tau \approx 1.8 \times 10^4$ s is the mean integration time per field, and $\Delta\nu \approx 7 \times 3.125$ MHz is the total bandwidth of one IF. The theoretical noise is $\sigma \approx 19$ μJy beam^{-1} for our choice of (u, v)-weighting. In practice, not all telescopes were available continuously and some images are limited by dynamic range. We measured actual rms fluctuations $\sigma \approx 21.5$ μJy beam^{-1} at the centers of most images and slightly higher values in images containing the strongest sources.

The final image is the weighted sum of the $m = 35$ individual images. Let b_i be the sky brightness at the location of any pixel from an individual image, not attenuated by the normalized primary power pattern. The weight W_i assigned to that pixel is the square of the normalized primary power pattern at that pixel; this weight is proportional to the square of the expected sensitivity. Thus, the brightness on the attenuated image is $W^{1/2} b_i$. Calculating the final image brightnesses from

$$B = \sum_{i=1}^{m} W_i^{1/2} (W_i^{1/2} b_i) / \sum_{i=1}^{m} W_i = \sum_{i=1}^{m} W_i b_i / \sum_{i=1}^{m} W_i$$

simultaneously maximizes the overall sensitivity and corrects for primary-beam attenuation. The pixel weights in the final image are

$$W = \sum_{i=1}^{m} W_i \, ,$$

and the local noise level should be proportional to $W^{-1/2}$. A pixel with $W = 1.00$ has the same theoretical sensitivity as the center of one individual image, and we blanked all pixels having $W < 0.64$ to truncate the edges of the weighted image. The distribution of pixel weights in the final blanked image is shown in Figure 2. The mean weight is $\langle W \rangle \approx 0.879$, so the rms noise averaged over the entire final image should be about $(21.5\ \mu\text{Jy}) \langle W \rangle^{-1/2} \approx 23\ \mu$Jy. The actual distribution of pixel brightnesses in the final image is shown as a logarithmic histogram in Figure 3. It is consistent with the superposition of a Gaussian noise distribution having rms amplitude $\sigma = 23.0$ μJy beam^{-1}, a weak negative-going tail caused by uncleaned sidelobes of strong sources, and a long positive-going tail representing genuine radio sources. The rms noise is within 10% of 23 μJy everywhere in the image except for

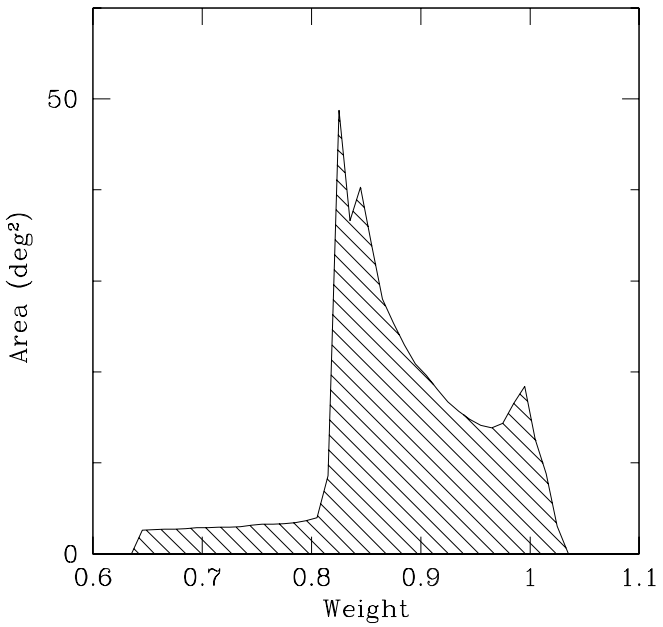

FIG. 2.—Statistical weight distribution of pixels in the VLA image truncated below $W = 0.64$.

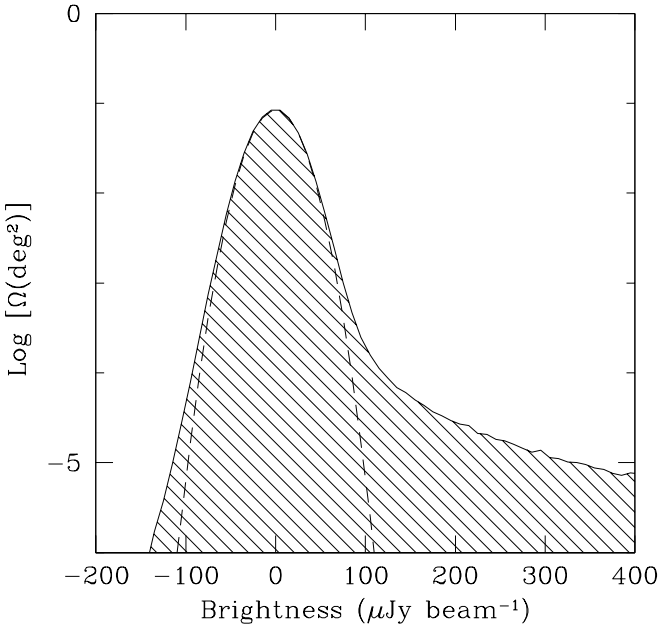

FIG. 3.—Pixel brightness distribution in the VLA image. The dashed curve corresponds to Gaussian noise, with an rms amplitude $\sigma = 23$ μJy beam^{-1}.

small regions near the strongest sources, where the cautious user should examine the postage-stamp images when estimating errors or upper limits.

3. RESULTS

A small portion of the final radio image is displayed in Figure 4. Most of the fainter sources are unresolved or only slightly resolved by the 5″ FWHM Gaussian restoring beam, but there are a few examples of extended double, triple, or more complex morphologies among the brighter sources, the triple source centered on $\alpha = 17^{h}17^{m}33^{s}.8$, $\delta = +67^{\circ}07'47''$, for example. Such a distribution of angular sizes and morphologies is expected in samples complete to $S \approx 115$ μJy (Condon 1989). Most sources slightly stronger than $S \sim 1$ mJy have 1.4 GHz spectral luminosities $L \sim 10^{24}$ W Hz^{-1} and are powered by low-luminosity active galactic nuclei. Their median angular size is greater than 5″, so many are well resolved. In contrast, significantly weaker sources are more likely to be powered by and coextensive with star formation in distant galaxies whose angular sizes are less than 5″.

Since most of the faint sources are not significantly resolved, most of the information in the image is well represented by a catalog of elliptical Gaussian components. The free parameters of each fitted Gaussian are peak brightness, right ascension, declination, FWHM major and minor diameters, and major-axis position angle. However, freely fitted diameters smaller than the restoring beamwidth are formally impossible. When they were found, they were fixed at 5″, and the fit was repeated. From the fitted parameters, we calculated the integrated flux density and deconvolved angular diameters (or upper limits). Uncertainties in these parameters were estimated from the same error propagation model for two-dimensional Gaussian fits used for the NVSS (Condon 1997; Condon et al. 1998) with assumed calibration uncertainties of 0.″1 in each coordinate and 3% in flux density. The final component catalog contains nearly all components brighter than $S_p = 115$ μJy beam$^{-1} \approx 5$ σ; the few that appear to be sidelobes near strong sources have been rejected. Most of the surviving components are astronomically distinct radio sources, but 105 groups of two or more components are probably extended radio sources. We labeled the components comprising these groups by their group numbers G001 through G105. Table 1 lists all 3565 radio components in right ascension order, and the individual columns are as follows:

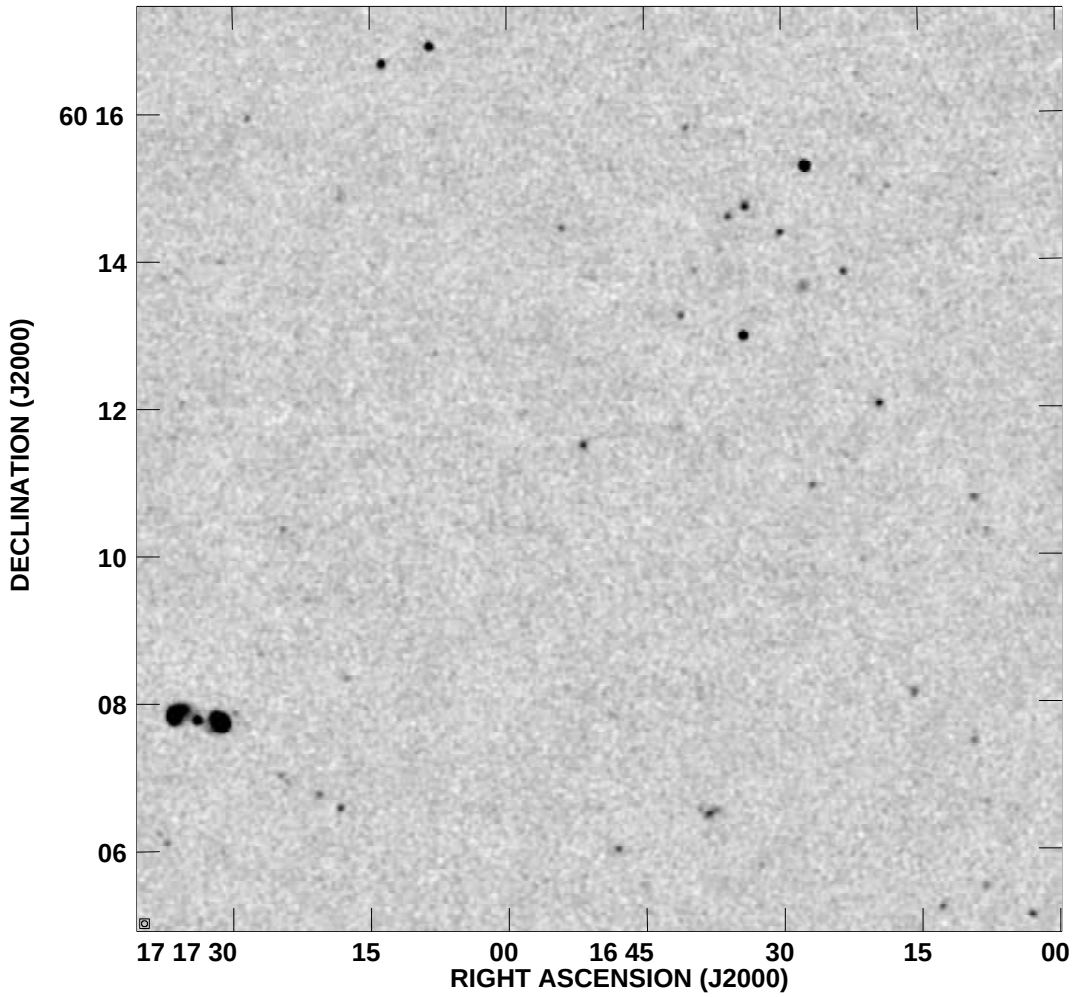

FIG. 4.—Subimage shows ≈1% of the FLS area with $\theta = 5.''0$ resolution (see the very small inset in the bottom left corner) and nearly uniform $\sigma \approx 23$ μJy noise.

TABLE 1
COMPONENT CATALOG

RIGHT ASCENSION (J2000.0) (1)	DECLINATION (J2000.0) (2)	FLUX DENSITY (mJy) (3)	MAJOR AXIS (arcsec) (4)	MINOR AXIS (arcsec) (5)	P.A. (deg) (6)	PIXEL		GROUP CODE (9)
						X (7)	*Y* (8)	
17 07 50.959 ± 0.032	+59 40 27.99 ± 0.21	0.721 ± 0.086	4.6 ± 0.6	3.1 ± 0.6	−66.5 ± 13.2	7171.90	4574.45	...
17 07 51.518 ± 0.054	+59 41 25.98 ± 0.33	0.213 ± 0.025	<5.1	<3.7	...	7167.61	4612.99	...
17 07 51.592 ± 0.046	+59 41 40.08 ± 0.34	0.198 ± 0.023	<3.8	<3.8	...	7166.88	4622.36	...
17 07 52.656 ± 0.036	+59 39 33.74 ± 0.26	0.269 ± 0.024	<3.4	<3.2	...	7164.72	4537.97	...
17 07 54.370 ± 0.030	+59 46 40.54 ± 0.27	0.358 ± 0.029	<4.5	<3.5	...	7145.26	4822.04	...

NOTES.—Table 1 is presented in its entirety in the electronic edition of the Astronomical Journal. A portion is shown here for guidance regarding its form and content.

Column (1): Right ascension (J2000.0) and its rms uncertainty.

Column (2): Declination (J2000.0) and its rms uncertainty.

Column (3): Integrated flux density (in millijanskys) and its rms uncertainty.

Column (4): Deconvolved FWHM major axis (in arcseconds) and its rms uncertainty, else a 98% confidence upper limit.

Column (5): Deconvolved FWHM minor axis (in arcseconds) and its rms uncertainty, else a 98% confidence upper limit.

Column (6): Major-axis position angle (in degrees east of north) and its rms uncertainty.

Column (7): *X*-pixel location in the final image.

Column (8): *Y*-pixel location in the final image.

Column (9): Group number for groups of components that appear to make up complex radio sources.

To avoid ambiguity, please refer to radio components in the FLS VLA catalog by their full IAU designations (Lortet, Borde, & Ochsenbein 1994) of the form FLSVLA Jhhmmss.s+ddmmss, where FLSVLA is the catalog acronym, "J" specifies the coordinate equinox J2000.0, hhmmss.s concatenates the hours, minutes, seconds, and truncated (not rounded) decimal seconds of right ascension, and +ddmmss represents the degrees, arcminutes, and truncated (not rounded) arcseconds of declination. Thus the radio component at J2000.0 $\alpha = 17^{h}07^{m}50\overset{s}{.}959$, $\delta = +59^{\circ}40'27\overset{''}{.}99$ should be called FLSVLA J170750.9+594027.

Our estimates for the positions and flux densities of the 105 multicomponent sources are given in Table 2. The columns of Table 2 are as follows:

Column (1): Component group number.

Column (2): Number of components in the group.

Column (3): Right ascension (J2000.0).

Column (4): Declination (J2000.0).

Column (5): Flux density (in millijanskys).

Column (6): Figure number of contour plot, if any.

Normally the positions listed in Table 2 are either the centroids of simple double sources or the fitted positions of central components in triples. The flux densities are the sums of the component flux densities for those groups that are well approximated by Gaussians. We estimated the flux densities of groups containing diffuse or complex emission by summing directly over the pixel brightness distributions. Using radio morphology alone to combine groups of components into astrophysically distinct sources is only educated guesswork, so these "sources" should be regarded as tentative and their resulting parameters as uncertain. Those complex sources whose brightness distributions are not well approximated by two elliptical Gaussians are plotted in Figures 5–13.[4]

Q. F. Yin was supported in part by Jet Propulsion Laboratory contract number 1234549.

[4] The radio image, component catalog, and user software for extracting postage-stamp subimages and browsing the catalog are available via the Web at http://www.cv.nrao.edu/sirtf_fls/ and http://sirtf.caltech.edu/SSC/fls.

TABLE 2

MULTICOMPONENT SOURCE CATALOG

Component Group (1)	Number of Components (2)	Right Ascension (J2000.0) (3)	Declination (J2000.0) (4)	Flux Density (mJy) (5)	Figure (6)
G001	2	17 08 15.08	+59 58 59.1	8.18	...
G002	4	17 08 17.42	+59 46 29.9	44.33	5*a*
G003	2	17 08 23.79	+59 59 06.3	1.22	...
G004	2	17 08 38.64	+59 44 03.9	23.24	5*b*
G005	2	17 08 43.05	+59 31 40.2	33.81	...
G006	2	17 08 46.65	+59 32 23.0	5.63	5*c*
G007	2	17 09 21.16	+60 01 30.4	3.89	...
G008	4	17 09 26.57	+59 39 36.6	38.77	5*d*
G009	2	17 09 42.49	+60 12 03.2	28.07	5*e*
G010	4	17 09 53.78	+59 48 38.2	1.79	5*f*
G011	2	17 09 56.33	+59 57 31.7	3.90	5*g*
G012	2	17 10 15.99	+59 20 18.5	14.89	5*h*
G013	2	17 10 33.24	+59 36 04.9	1.61	...
G014	2	17 10 44.33	+59 54 56.7	1.60	6*a*
G015	6	17 11 05.32	+59 57 50.2	3.16	6*b*
G016	2	17 11 15.99	+59 56 31.7	28.77	...
G017	2	17 11 17.85	+60 19 28.0	41.95	6*c*
G018	3	17 11 18.34	+59 12 12.6	2.23	...
G019	2	17 11 31.77	+59 39 17.0	26.33	...
G020	7	17 11 45.40	+60 08 08.7	23.64	6*d*
G021	2	17 11 47.89	+58 40 11.5	12.08	6*e*
G022	2	17 12 06.54	+58 52 16.2	1.92	...
G023	5	17 12 13.86	+59 17 24.1	6.56	7*a*
G024	2	17 12 17.45	+59 00 51.6	9.21	7*b*
G025	2	17 12 21.16	+58 33 00.3	59.85	7*c*
G026	13	17 12 28.47	+59 56 34.3	31.57	7*d*
G027	2	17 12 37.92	+59 05 06.4	3.32	...
G028	2	17 12 39.49	+58 41 45.2	1.49	...
G029	2	17 12 45.07	+58 59 47.8	4.80	7*e*
G030	3	17 12 48.11	+59 14 31.1	12.86	7*f*
G031	5	17 13 19.41	+59 20 02.8	5.38	7*g*
G032	2	17 13 40.84	+59 49 19.7	0.86	...
G033	3	17 13 43.04	+58 45 36.8	6.91	7*h*
G034	2	17 13 50.03	+58 27 43.1	2.61	...
G035	2	17 14 02.72	+58 46 22.4	19.82	8*a*
G036	2	17 14 14.14	+59 47 56.0	15.90	8*b*
G037	5	17 14 30.85	+60 36 06.4	37.51	8*c*
G038	2	17 14 35.83	+59 47 20.9	11.74	8*d*
G039	3	17 14 40.33	+60 04 01.3	30.31	8*e*
G040	2	17 14 46.02	+58 35 19.5	1.22	...
G041	2	17 14 47.74	+58 53 50.8	8.26	...
G042	2	17 14 52.13	+59 12 36.4	3.73	...
G043	5	17 14 57.85	+59 15 39.7	25.02	8*f*
G044	2	17 15 08.96	+58 45 27.0	10.11	8*g*
G045	2	17 15 46.93	+59 17 06.0	17.53	...
G046	2	17 16 22.70	+59 15 30.8	14.75	...
G047	9	17 16 39.36	+59 15 13.4	19.65	8*h*
G048	2	17 16 42.95	+60 23 24.4	2.79	...
G049	2	17 16 51.66	+58 12 50.3	10.14	9*a*
G050	3	17 17 03.00	+60 34 38.4	3.61	9*b*
G051	2	17 17 19.58	+60 18 17.0	18.28	9*c*
G052	4	17 17 33.80	+60 07 47.0	20.99	9*d*
G053	2	17 17 44.25	+59 18 18.4	2.42	9*e*
G054	3	17 18 21.91	+59 46 59.2	0.64	...
G055	2	17 18 29.66	+58 09 13.4	9.64	9*f*
G056	3	17 18 29.48	+60 52 04.0	34.06	9*g*
G057	5	17 18 31.63	+60 18 28.1	2.31	9*h*
G058	8	17 18 41.10	+60 36 28.1	43.80	10*a*
G059	2	17 18 58.92	+58 27 32.5	3.77	...
G060	2	17 19 21.12	+59 09 39.4	4.59	...
G061	3	17 19 27.24	+59 59 11.3	1.16	...
G062	2	17 19 43.86	+58 17 29.5	2.37	...
G063	3	17 19 52.37	+60 14 34.7	103.53	...

TABLE 2—*Continued*

Component Group (1)	Number of Components (2)	Right Ascension (J2000.0) (3)	Declination (J2000.0) (4)	Flux Density (mJy) (5)	Figure (6)
G064	3	17 19 53.26	+58 52 19.6	6.44	10*b*
G065	2	17 19 56.18	+59 38 36.0	42.81	...
G066	3	17 20 04.01	+58 38 28.0	251.95	...
G067	5	17 20 10.26	+59 24 15.2	35.24	10*c*
G068	3	17 20 09.72	+60 08 02.5	8.51	10*d*
G069	4	17 20 17.18	+58 20 32.2	9.85	10*e*
G070	3	17 20 28.26	+59 13 41.6	85.56	10*f*
G071	2	17 20 30.76	+58 23 00.9	17.05	10*g*
G072	2	17 20 53.71	+60 29 56.9	1.04	...
G073	10	17 21 10.96	+60 12 57.6	57.35	11*a*
G074	2	17 21 12.37	+59 22 16.2	23.74	11*b*
G075	3	17 21 16.59	+60 04 06.3	4.22	11*c*
G076	2	17 21 19.20	+59 37 32.6	38.18	11*d*
G077	3	17 21 27.32	+60 05 59.0	1.94	11*e*
G078	3	17 21 30.83	+58 25 58.4	2.77	...
G079	2	17 21 47.82	+60 15 48.7	0.64	...
G080	3	17 21 48.23	+60 25 31.2	65.87	11*f*
G081	2	17 21 57.73	+59 15 22.6	8.88	11*g*
G082	3	17 22 00.58	+60 24 04.2	6.73	11*h*
G083	4	17 22 05.48	+59 06 50.5	5.27	12*a*
G084	4	17 22 15.28	+60 22 59.3	48.53	12*b*
G085	2	17 22 16.36	+58 56 56.3	0.79	...
G086	2	17 22 19.59	+59 04 35.0	5.55	12*c*
G087	2	17 22 45.71	+60 00 04.7	93.14	12*d*
G088	2	17 22 49.55	+60 26 42.0	2.03	...
G089	2	17 22 52.58	+60 07 45.5	0.96	...
G090	2	17 23 02.90	+60 29 11.9	7.05	12*e*
G091	3	17 23 31.95	+60 15 27.2	3.11	12*f*
G092	4	17 23 33.00	+58 50 35.0	1.70	12*g*
G093	4	17 23 34.73	+60 19 48.2	4.37	12*h*
G094	4	17 23 36.85	+59 37 16.1	23.68	12*i*
G095	5	17 24 07.77	+59 19 05.6	9.36	13*a*
G096	2	17 24 34.06	+60 11 31.3	60.96	...
G097	7	17 24 39.34	+59 20 44.1	6.84	13*b*
G098	2	17 24 44.45	+58 42 16.5	8.58	...
G099	2	17 24 54.63	+59 13 25.0	2.44	...
G100	3	17 24 55.39	+60 24 25.1	59.71	13*c*
G101	2	17 25 51.47	+59 05 40.5	1.16	13*d*
G102	5	17 26 25.84	+59 27 03.2	2.76	13*e*
G103	5	17 26 59.48	+59 40 18.0	37.83	13*f*
G104	2	17 27 00.54	+59 14 16.2	4.06	...
G105	3	17 27 40.73	+58 57 52.7	1.36	...

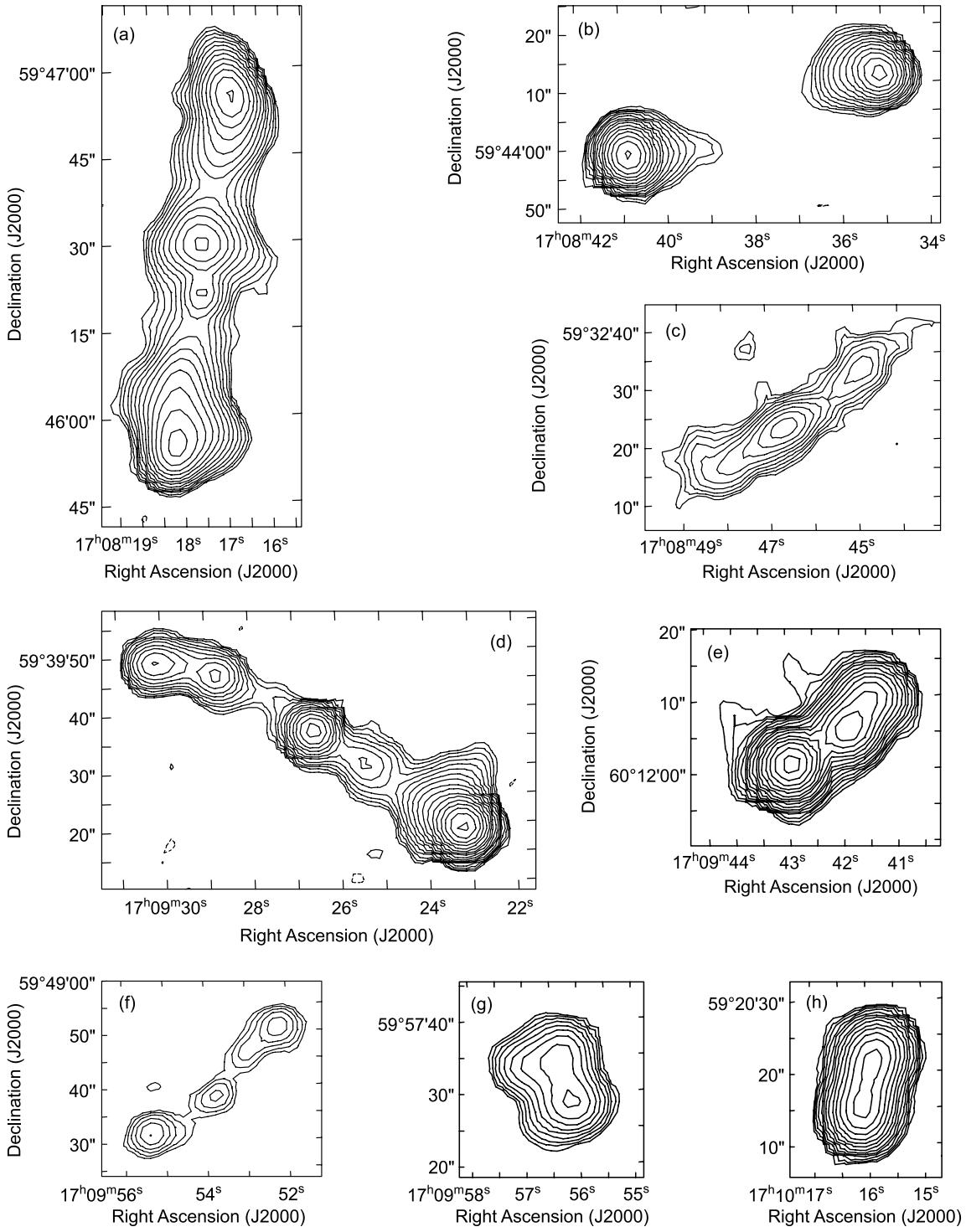

FIG. 5.—Complex sources for (*a*) G002, (*b*) G004, (*c*) G006, (*d*) G008, (*e*) G009, (*f*) G010, (*g*) G011, and (*h*) G012. Contours are plotted at $\pm$ 50 μJy beam^{-1} $\times$ $2^{1/2}$, 2^{1}, $2^{3/2}$, 2^{2}, ….

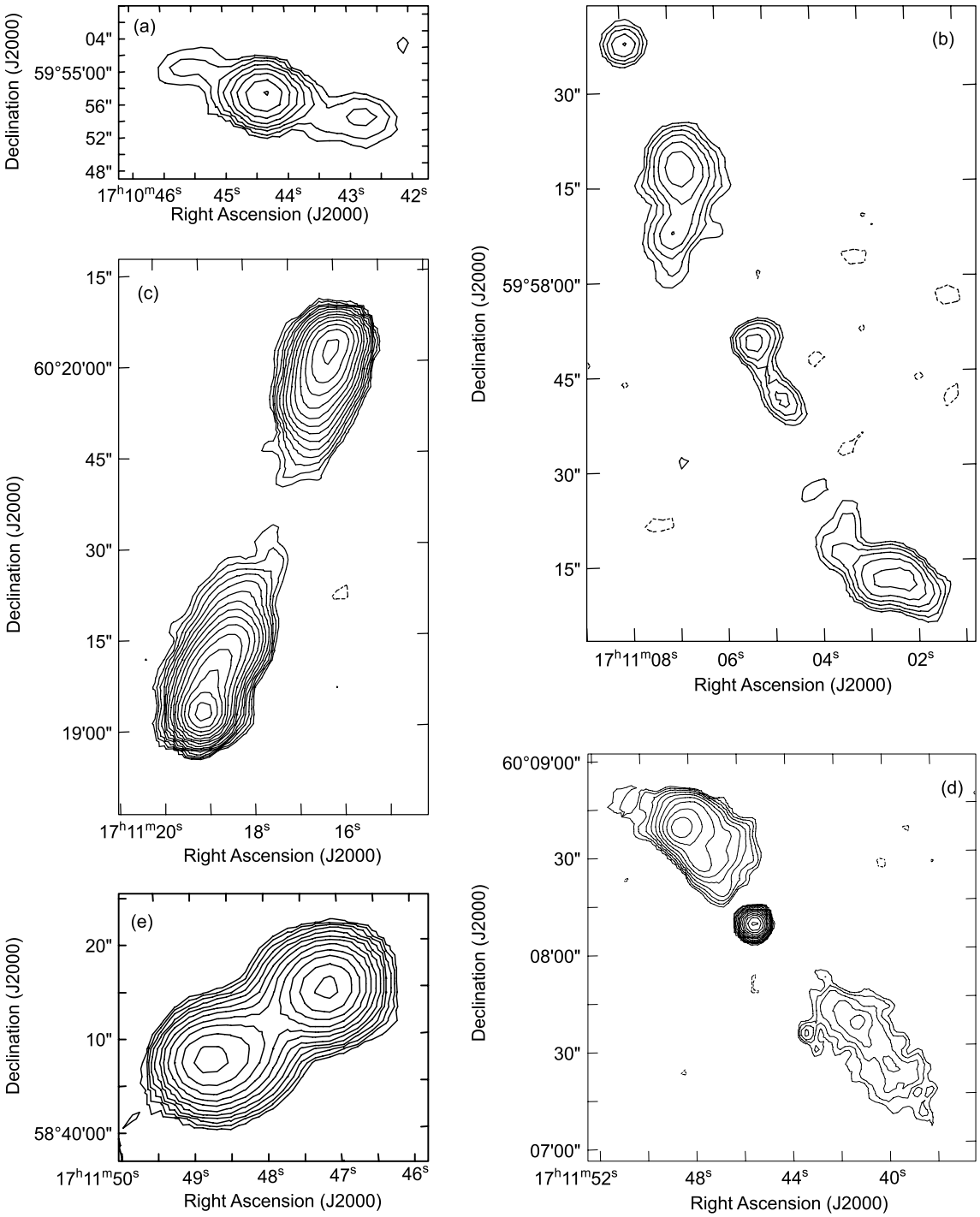

FIG. 6.—Same as Fig. 5, but for (*a*) G014, (*b*) G015, (*c*) G017, (*d*) G020, and (*e*) G021

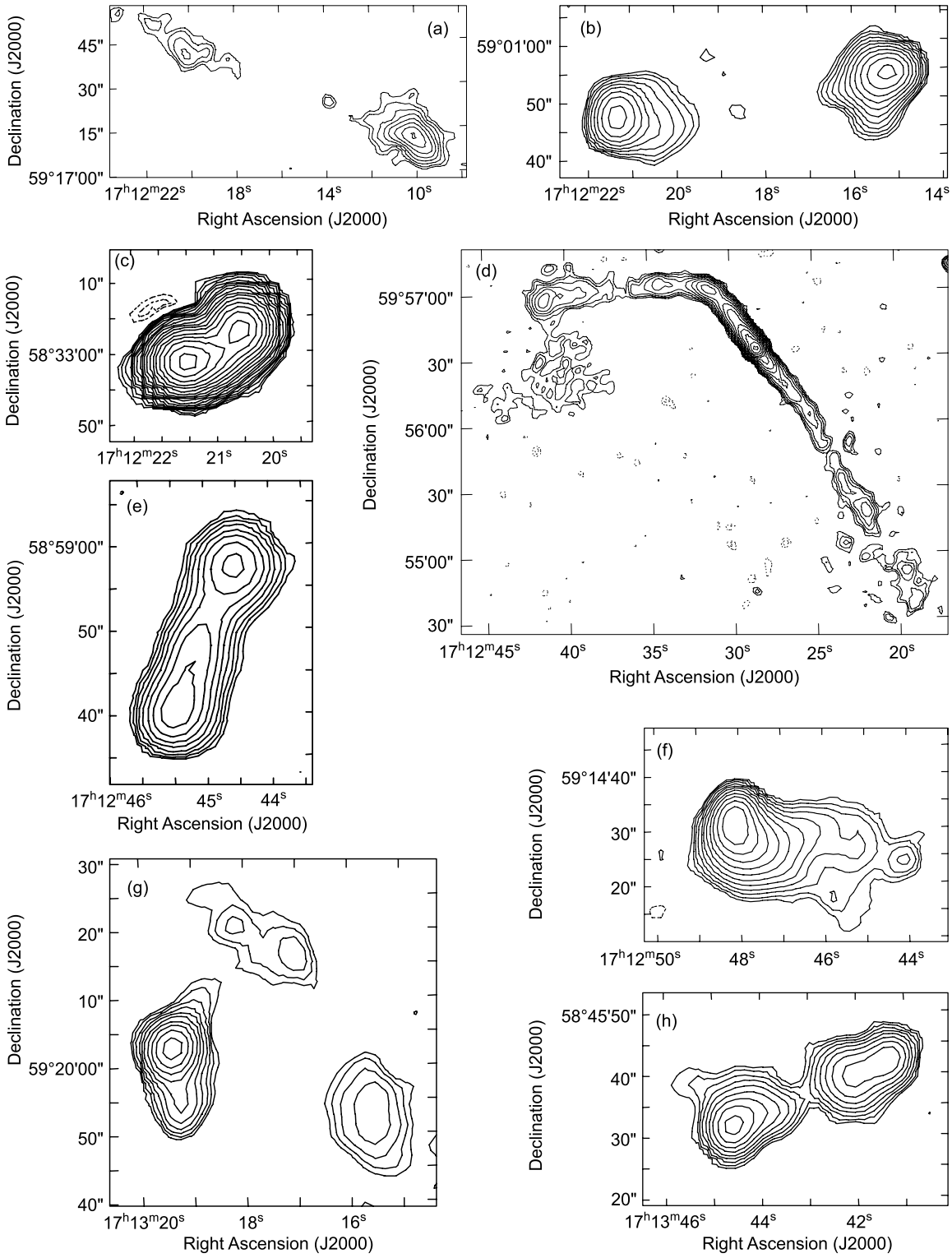

FIG. 7.—Same as Fig. 5, but for (*a*) G023, (*b*) G024, (*c*) G025, (*d*) G026, (*e*) G029, (*f*) G030, (*g*) G031, and (*h*) G033

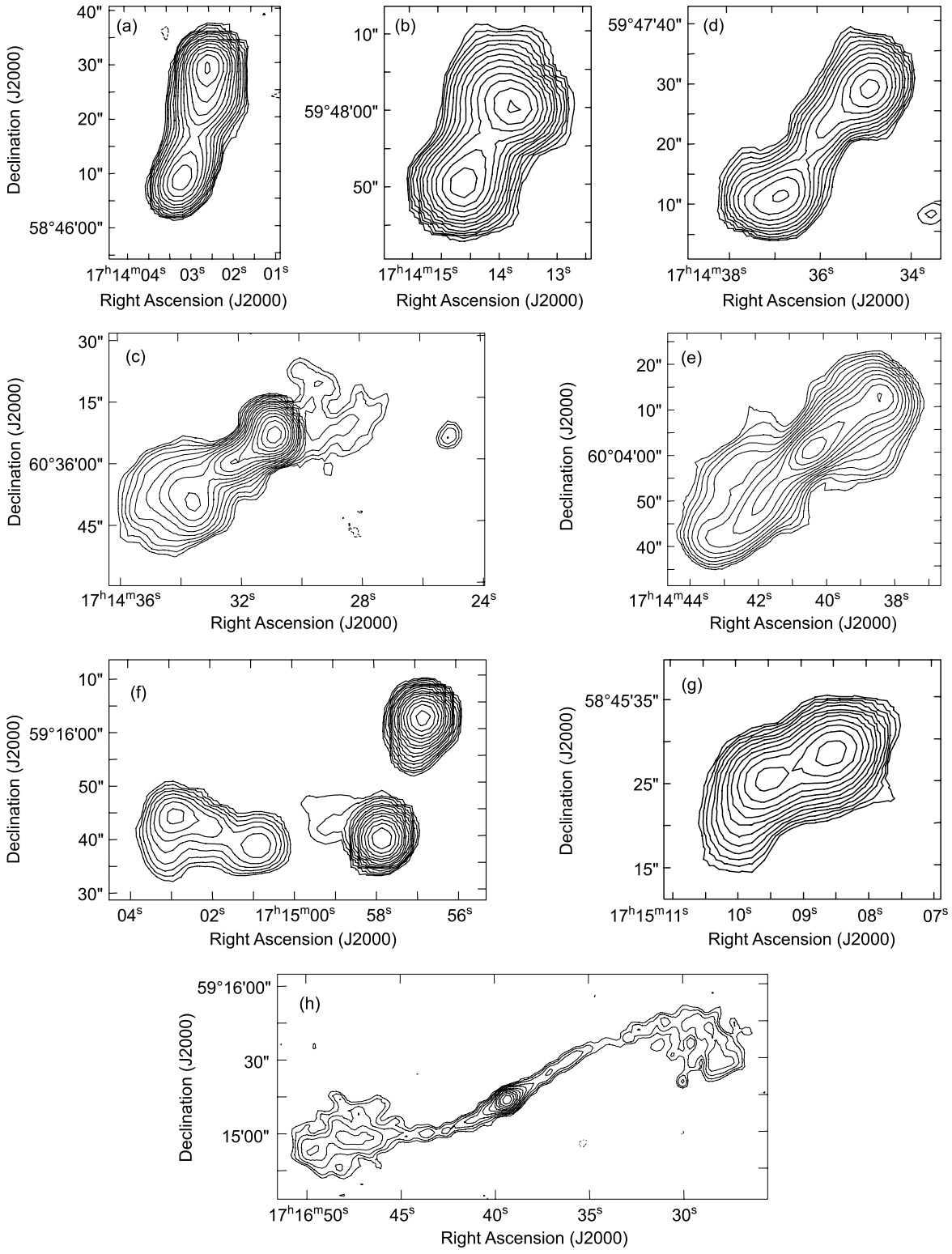

FIG. 8.—Same as Fig. 5, but for (*a*) G035, (*b*) G036, (*c*) G037, (*d*) G038, (*e*) G039, (*f*) G043, (*g*) G044, and (*h*) G047

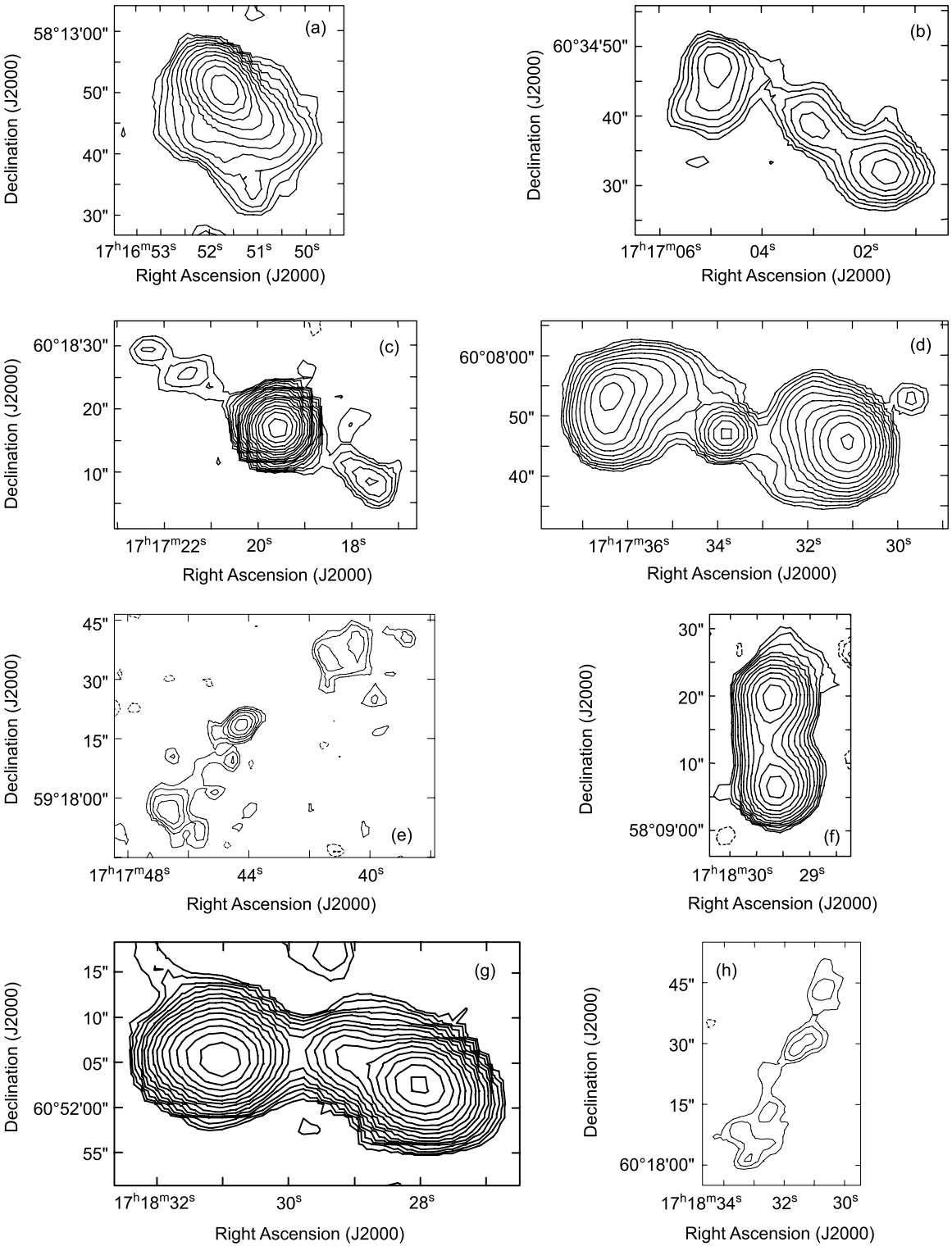

FIG. 9.—Same as Fig. 5, but for (*a*) G049, (*b*) G050, (*c*) G051, (*d*) G052, (*e*) G053, (*f*) G055, (*g*) G056, and (*h*) G057

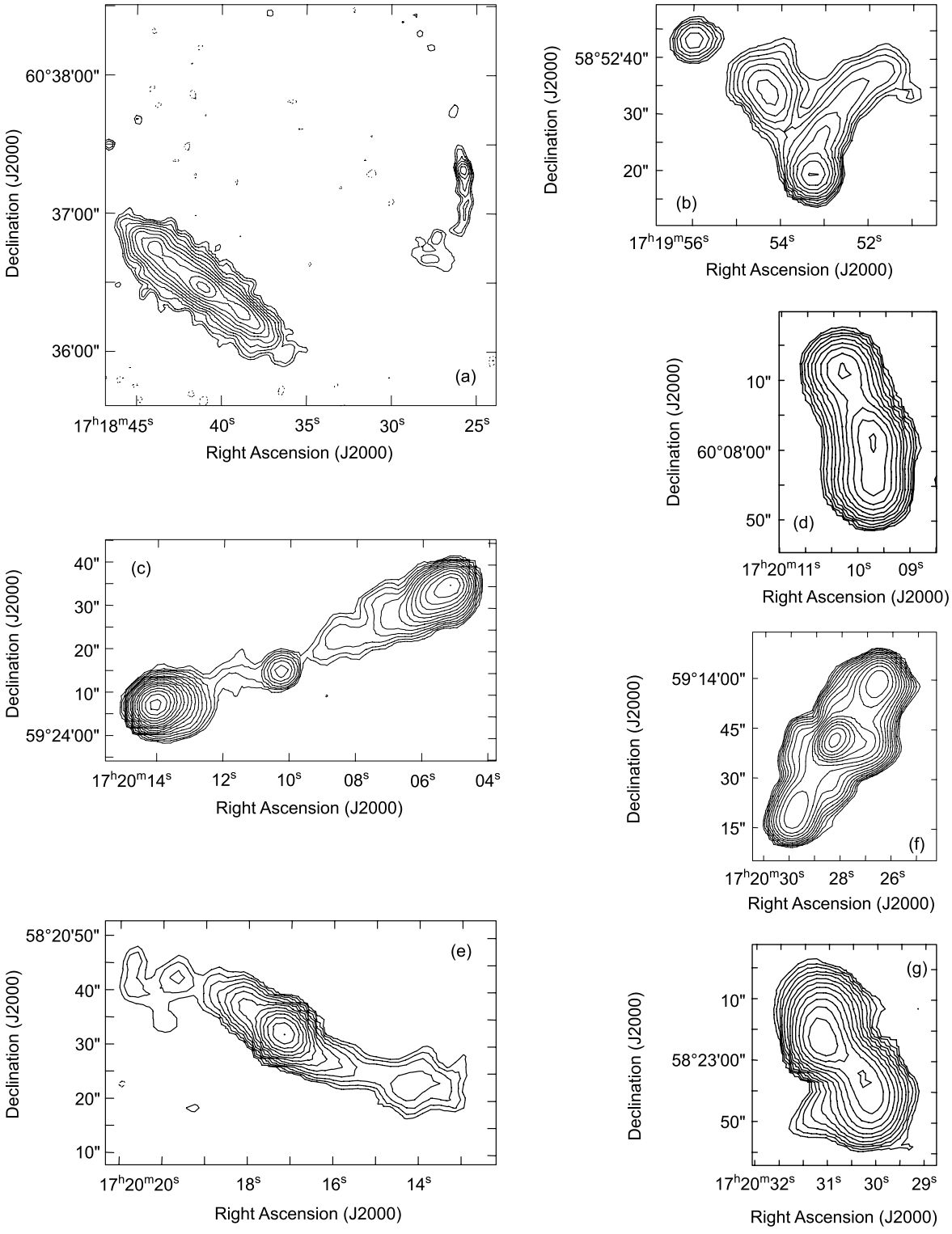

FIG. 10.—Same as Fig. 5, but for (*a*) G058, (*b*) G064, (*c*) G067, (*d*) G068, (*e*) G069, (*f*) G070, and (*g*) G071

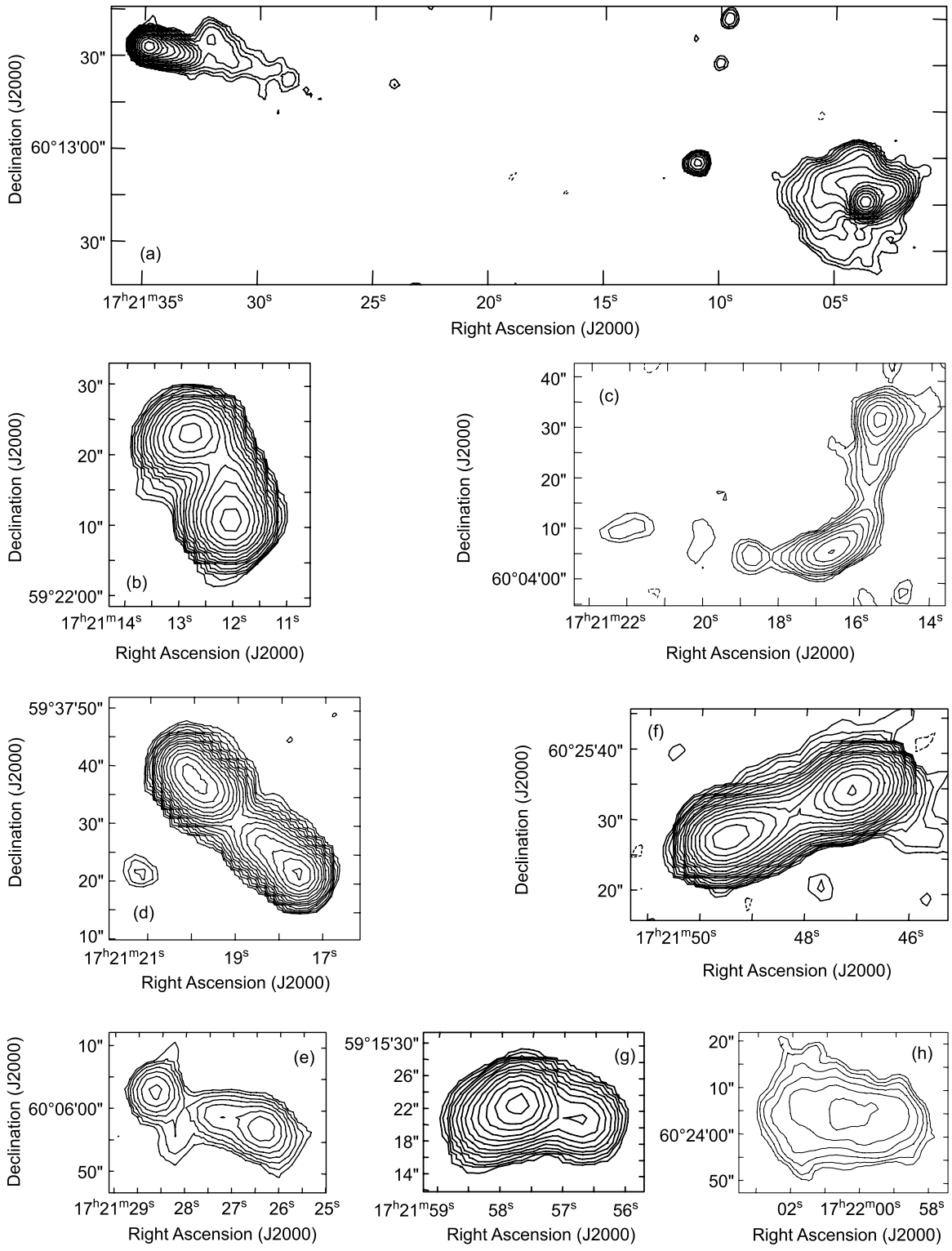

FIG. 11.—Same as Fig. 5, but for (*a*) G073, (*b*) G074, (*c*) G075, (*d*) G076, (*e*) G077, (*f*) G080, (*g*), G081, and (*h*) G082

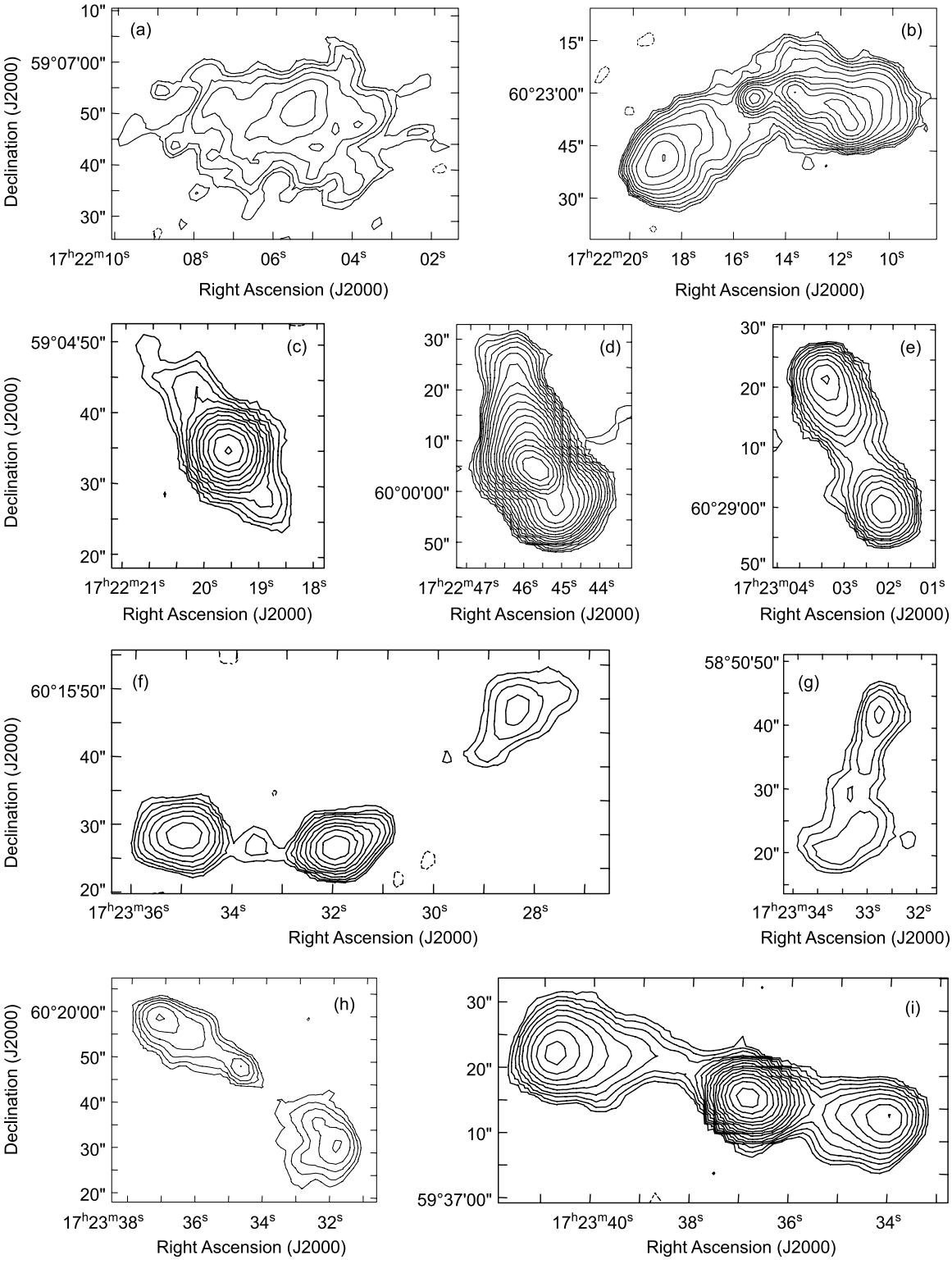

FIG. 12.—Same as Fig. 5, but for (*a*) G083, (*b*) G084, (*c*) G086, (*d*) G087, (*e*) G090, (*f*) G091, (*g*) G0921, (*h*) G093, and (*i*) G094

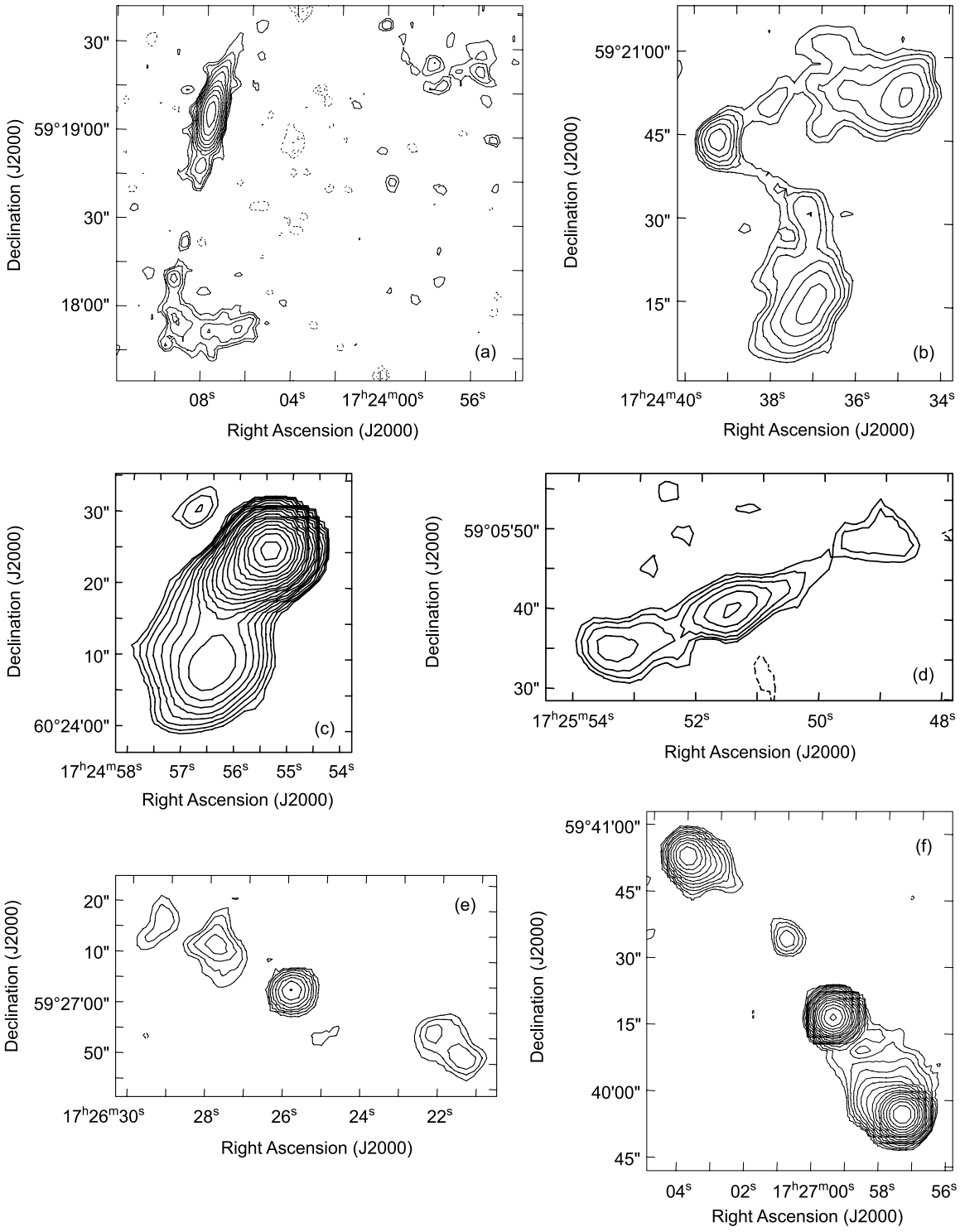

FIG. 13.—Same as Fig. 5, but for (*a*) G095, (*b*) G097, (*c*) G100, (*d*) G101, (*e*) G102, and (*f*) G103

REFERENCES

Condon, J. J. 1989, ApJ, 338, 13
———. 1997, PASP, 109, 166
Condon, J. J., Anderson, M. A., & Helou, G. 1991, ApJ, 376, 95
Condon, J. J., Cotton, W. D., Greisen, E. W., Yin, Q. F., Perley, R. A., Taylor, G. B., & Broderick, J. J. 1998, AJ, 115, 1693
Crane, P. C., & Napier, P. J. 1989, in ASP Conf. Ser. 6, Synthesis Imaging in Radio Astronomy, ed. R. A. Perley, F. R. Schwab, & A. H. Bridle (San Francisco: ASP), 139
Lortet, M.-C., Borde, S., & Ochsenbein, F. 1994, A&AS, 107, 193
Puget, J. L., et al. 1999, A&A, 345, 29
Schlegel, D. J., Finkbeiner, D. P., & Davis, M. 1998, ApJ, 500, 525
Soifer, B. T., Boehmer, L., Neugebauer, G., & Sanders, D. B. 1989, AJ, 98, 766